International Journal of Minerals, Metallurgy and Materials
Volume 27, Number 4, April 2020, Page 483
https://doi.org/10.1007/s12613-019-1916-4

Mechanical properties and wear resistance of ultrafine bainitic steel under low austempering temperature

Wei Liu[1)], *You-hui Jiang*[1)], *Hui Guo*[2)], *Yue Zhang*[1)], *Ai-min Zhao*[1)], *and Yao Huang*[3)]

1) Collaborative Innovation Center of Steel Technology, University of Science and Technology Beijing, Beijing 100083, China
2) School of Mechanical Engineering, Weifang University of Science and Technology, Shouguang 262700, China
3) China Electric Power Research Institute, Beijing 100192, China
(Received: 21 June 2019; revised: 11 September 2019; accepted: 16 September 2019)

Abstract: The mechanical properties and wear resistance of the ultrafine bainitic steel austempered at various temperatures were investigated. Scanning electron microscopy (SEM) and X-ray diffraction were used to analyze the microstructure. The worn surfaces were observed via laser scanning confocal microscopy and SEM. Results indicated that, under low austempering temperatures, the mechanical properties differed, and the wear resistance remained basically unchanged. The tensile strength of the samples was above 1800 MPa, but only one sample austempered at 230°C had an elongation of more than 10%. The weight loss of samples was approximately linear with the cycles of wear and nonlinear with the loads. The samples showed little difference in wear resistance at different isothermal temperatures, whereas the thickness of their deformed layers varied greatly. The results are related to the initial hardness of the sample and the stability of the retained austenite. Meanwhile, the experimental results showed that the effect of austempering temperature on the wear resistance of ultrafine bainitic steel can be neglected under low applied loads and low austempering temperature.

Keywords: bainitic steel; mechanical properties; wear resistance; austempering temperature

1. Introduction

Ultrafine bainitic steel, developed by Bhadeshia and their co-workers [1], has a multiphase structure comprising extremely fine bainitic ferrite and carbon-rich retained austenite formed by austempering at 125–350°C [1−4]. The former provides ultrahigh strength (1.2–2.6 GPa) [5−8], and the latter offers sufficient toughness for ultrafine bainitic steels (30–50 MPa·m$^{1/2}$) [8−10]. This combination of strength and toughness has attracted the attention of scholars.

In addition to its mechanical properties, the wear resistance of ultrafine bainitic steels is also of significant interest. In recent years, extensive research has been conducted on the wear resistance of ultrafine bainitic steels, such as two-body abrasive wear [11−12], three-body abrasive wear [13−14], dry sliding wear [15], rolling/sliding wear [16−17], repeated frictional sliding [18−19], etc. Long *et al.* [20] studied the wear resistance of carbide-free bainitic steels, finding that carbide-free bainite exhibited higher wear resistance under high wear loading because of the increased hardness of the sample surface by the strain-induced martensitic transformation from retained austenite. Das Bakshi *et al.* [13] studied the wear resistance of three microstructures under a three-body abrasive. They found that nanostructured bainite was more resistant to abrasion than the other two types of microstructure, including fine pearlite and martensite. This is, perhaps, because of austenitization and the martensite transformation of the surface layer during abrasion. Hasan *et al.* [16] found that carbide-free bainitic rail steel had a higher wear resistance than pearlitic rail steel and that the wear resistance increased with increasing retained austenite content and decreasing bainitic ferrite lath thickness. The ultrafine bainitic structure, which is formed at low austempering temperatures, has, therefore, displayed satisfactory wear resistance.

Prior studies [11,19] have shown that, the lower the aus-

Corresponding author: Ai-min Zhao E-mail: aimin.zhao@ustb.edu.cn

tempering temperature, the better the wear resistance of the ultrafine bainitic steel. Because this finding was obtained at a higher temperature gradient (Ms + 50°C to Ms + 150°C, Ms: martensite start temperature), it is unclear whether the wear resistance of the ultrafine bainite obtained under a lower temperature gradient (Ms to Ms + 50°C) would also display these properties. Therefore, a new composition of high-carbon, low-alloy ultrafine bainitic steel was designed and austempered between Ms + 5°C and Ms + 50°C for this study. Moreover, the wear resistance and wear mechanism of the new bainite steel under two-body wear were studied. Additionally, the effect of austempering temperature and applied load on the wear resistance was investigated.

2. Experimental

The chemical composition of the experimental steel used in this paper was 0.70C–2.47Si–1.18Mn–0.87Al (wt%). The steel was melted into an ingot of 20 kg by a vacuum medium frequency induction melting furnace. After forged, the steel billets were homogenized at 1200°C for 2 h; subsequently, the steel billets were rolled into a thickness of 6 mm, and finally cooled to ambient air temperature. The austenite formation temperature (Ac1 and Ac3) and Ms temperature were measured using a cylindrical sample (ϕ3 mm × 10 mm). The corresponding temperatures were 782, 853, and 185°C, respectively. The rolled steels were austenitized at 950°C for 30 min, followed by cooling to 190, 210, and 230°C for 48, 36, and 24 h, respectively, as shown in Fig. 1.

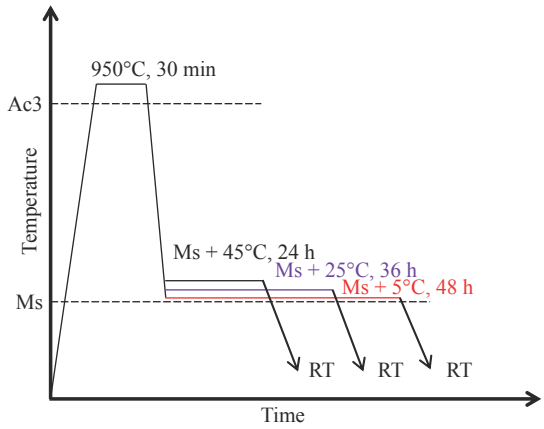

Fig. 1. Schematic diagram of austempering treatments. Ac3 is the austenite formation temperature, Ms is the martensite start temperature, and RT represents room temperature.

A ZEISS ULTRA 55-type field emission scanning electron microscope (FE-SEM), operating at 20 kV, was used to observe the microstructural morphology and phase distribution of the steel specimens. X-ray diffraction (XRD) was used to measure the volume fraction of the retained austenite (RA). The instrument was operated at 40 kV and a current of 150 mA with Cu K_α radiation. The 2θ scanning angles were varied from 45° to 95° with a stepping angle of 0.05° and a counting time of 1.2 s per step using 10 mm × 10 mm specimens. The RA content was measured by measuring the integrated intensities of the $(200)_\gamma$, $(220)_\gamma$, $(311)_\gamma$, $(200)_\alpha$, and $(211)_\alpha$ peaks [21]. The film-like RA content could be estimated using the Eq. (1) [22].

$$\frac{V_r^f}{V_r^b} = \frac{0.15V_{BF}}{V_r - 0.15V_{BF}} \tag{1}$$

where V_r^f, V_r^b, V_{BF}, and V_r represent the volume fraction of film-like retained austenite, blocky retained austenite, bainitic ferrite, and retained austenite, respectively.

Tensile properties were tested using an MTS 810 electronic universal testing machine with a crosshead speed of 1.0 mm·min^{-1} at room temperature. Samples were prepared with a gauge length of 25 mm and a width of 6 mm. The true stress–strain curves were converted based on the engineering stress–strain curves, and strain hardening was characterized by the instantaneous work-hardening coefficient (n), which was calculated from the true stress–strain curve as shown in Eq. (2).

$$n = \frac{d\ln\sigma}{d\ln\varepsilon} \tag{2}$$

where σ and ε are the true stress and true strain, respectively.

The equipment used in the two-body abrasion testing was an ML-100 abrasive wear testing machine. The rotation rate of the disk and a constant feed of samples were 60 r/min and 3 mm/r, respectively, as shown in Fig. 2. Applied loads used in the wear test were 5, 10, and 15 N. Cylindrical samples (ϕ3 mm × 10 mm) cut from the austempered samples were used to wear the experiments. The medium used for the abrasive wear test was 200 grit SiC paper (particle size: 75 μm). The wear test was stopped every 200 cycles, and weight loss of the samples was recorded using

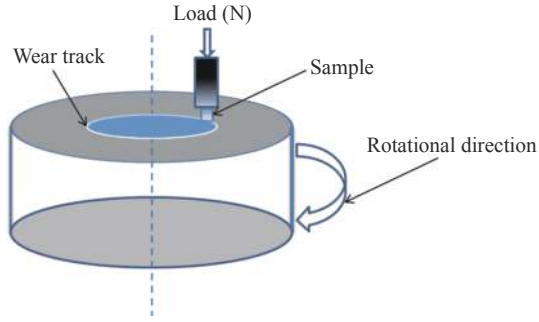

Fig. 2. Schematic diagram of wear tests.

an analytical balance (accuracy of 10^{-4} g). The total number of wear cycles was 600 rotations. Worn samples under each test condition were tested at least five times.

3. Results and discussion

3.1. Microstructure characterization

Fig. 3 shows the SEM images of the microstructures of ultrafine bainitic steels under different austempering temperatures. The microstructure for all heat treatments consisted of bainitic ferrite (BF) and RA. Precipitation of carbide was not observed in the microstructure because of the addition of Si [23]. According to the formula [24], $L_T = \pi t/2$, L_T is the mean linear intercept normal to the length of the plates, and t is the true thickness of the plates. The mean plate thicknesses (t) of BF are 49.3 ± 2.5, 58.2 ± 3.3, and 63.4 ± 3.3 nm, austempered at 190, 210, and 230°C, respectively (defined as 190-sample, 210-sample, and 230-sample). Untransformed austenite presented as blocky (prior austenite boundaries and between bainitic sheaves) and film-like (between BF plates) structures at ambient-temperature. The film-like retained austenite (FRA) was of great benefit when improving the toughness of the ultra-fine bainitic steel. Compared with FRA, the blocky retained austenite (BRA) was more inclined to transform into brittle martensite, which reduced the toughness of the ultrafine bainite steels under residual stresses or external forces [25]. The BRA dimension of the 190-sample was smaller than that of the other two samples, as shown in Fig. 3.

3.2. Mechanical properties

Fig. 4(a) represents the engineering stress−strain, and the measured tensile properties are enumerated in Table 1. The 230-sample displayed the lowest yield ($\sigma_{0.2}$) and tensile (σ_b)

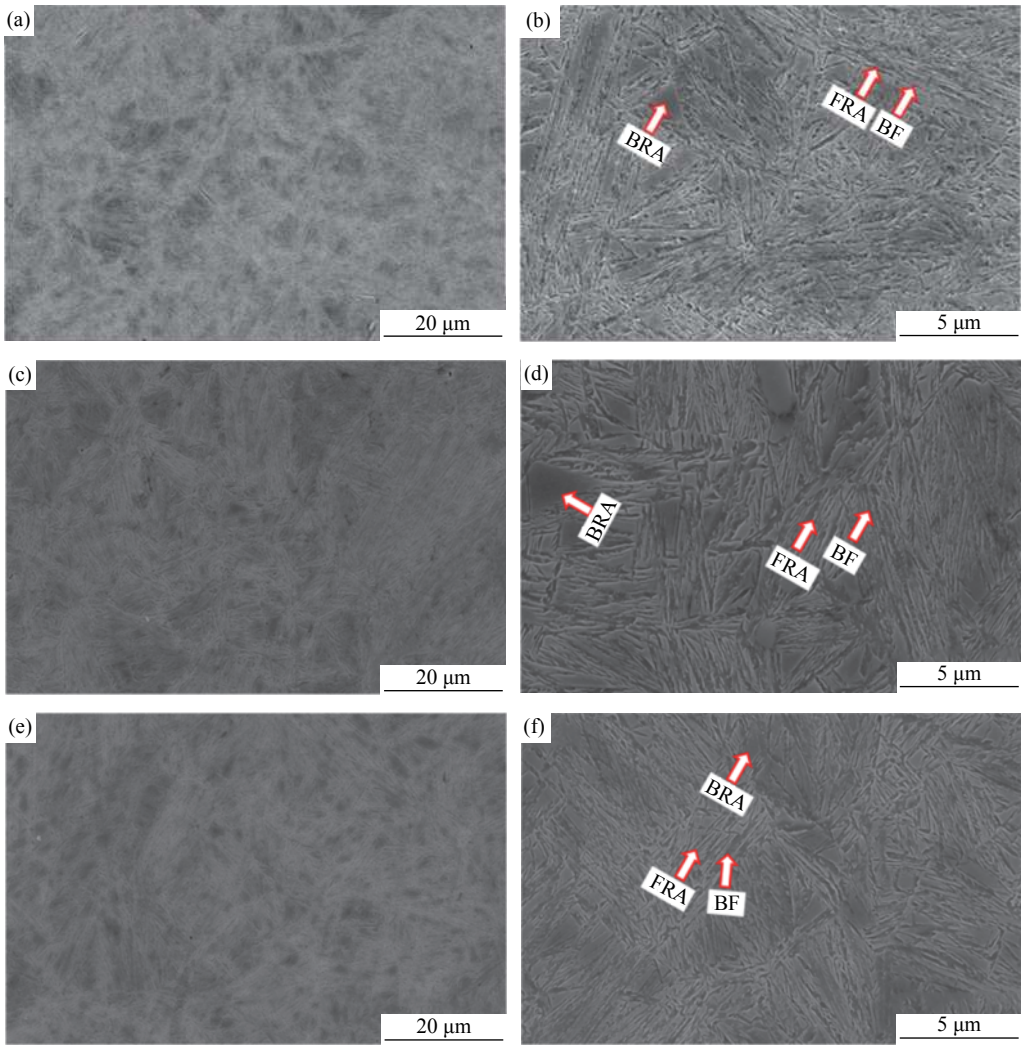

Fig. 3. SEM images of ultrafine bainitic steels austempered at different temperatures: (a, b) 190°C; (c, d) 210°C; (e, f) 230°C. BF, RFA, and BRA represent bainitic ferrite, film-like retained austenite, and blocky retained austenite, respectively.

strengths (1338 and 1846 MPa, respectively) and the highest elongation (10.93%). The yield and tensile strengths increased with decreasing austempering temperature, except for the tensile strength of the 210-sample, whereas the total elongation was the lowest in the 190-sample. Fig. 4(b) shows the true-strain and hardening index (n) curves. The 190-sample and 210-sample broke suddenly at low strain; the hardening index at that point was higher than for the 230-sample. Necking occurred in the 230-sample before fracture.

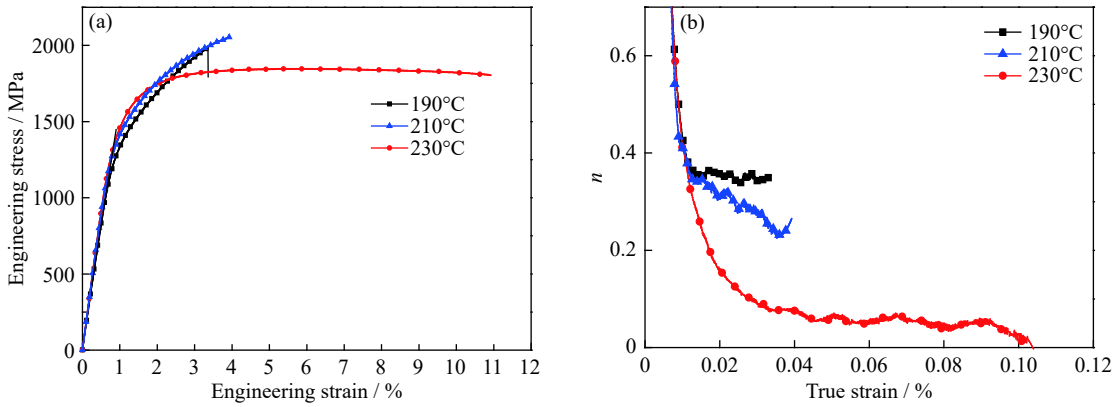

Fig. 4. Tensile properties and hardening index (n) curves: (a) engineering stress–strain curves; (b) true-strain vs. n curves of three samples in ambient temperature.

Table 1. Mechanical properties of the three samples

Sample	YS ($\sigma_{0.2}$) / MPa	UTS (σ_b) / MPa	TEL / %	Hardness, $HV_{1.0}$
190-sample	1523 ± 15	1985 ± 15	3.4 ± 0.17	673 ± 20
210-sample	1430 ± 13	2053 ± 13	3.9 ± 0.19	645 ± 21
230-sample	1338 ± 12	1846 ± 12	10.9 ± 0.6	593 ± 17

Note: YS, UTS, and TEL stand for yield strength, ultimate tensile strength, and total elongation, respectively.

It is well-known that nanoscale BF provides high strength for ultrafine bainitic steel. The strength (σ) is primarily controlled by the bainitic plate thickness (i.e., $\sigma = 115/(2t)$ [26]). As the austempering temperature decreases, the BF becomes thinner. BF thicknesses in the 190- and 230-samples were 49.3 ± 2.5 and 63.4 ± 3.3 nm, respectively. Dislocation density in the microstructure was also a factor affecting strength. After paraequilibrium nucleation, the ferrite plate grew through a shearing mechanism. During this process, austenite produced high-density dislocations to accommodate strain. The lower the bainite transformation temperature, the higher the strength of the parent austenite [27]. Dislocation density in the microstructure of the 190-sample was higher than that in the 230-sample. In summary, the ultimate tensile strength (UTS) of the 190- and 210-samples was higher than that of the 230-sample.

It is known that the amount, morphology, and distribution of RA are significant factors influencing the mechanical properties of steel. The volume fractions of RA were measured by XRD before and after the tensile test, as shown in Fig. 5. The RA contents of the three samples before and after stretching were >20vol% and 6−7.5vol%, respectively. It can be seen that the austenite to martensite transformation (TRIP effect) occurred in all samples during the tensile test. The question then arose as to why the elongations of the 190- and 210-samples were so low. This was attributed to the stability of the RA. The dimension and morphology of the RA had an important influence on the properties of the experimental steel. First, as the austempering temperature

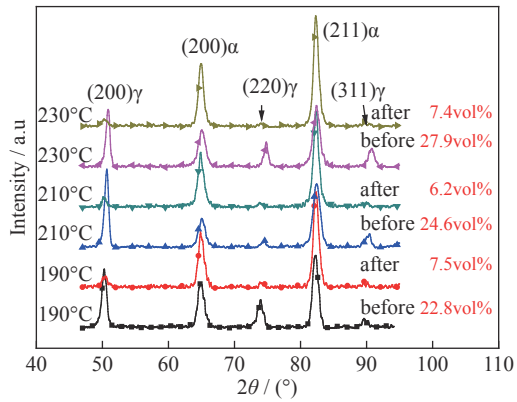

Fig. 5. X-ray diffraction (XRD) patterns and RA contents of three samples (austempered at 190, 210, and 230°C) before and after tensile experiments. RA means retained austenite.

decreased, the thickness of the BF and FRA decreased. The possibility of FRA producing a TRIP effect during the tension was reduced. Second, large amounts of BRA were transformed into martensite at low strain [28]. Third, BRA was liable to crack. These reasons could explain why the UTS of the 210-sample was higher than that of the 190-sample.

Typical SEM images of the tensile fracture surface of the 190- and 230-samples are shown in Fig. 6. The macroscopic fracture morphology of the samples was a river-like pattern, as shown in Figs. 6(a) and 6(b). The fracture surface was composed of number of cleavage facets and some tearing edges, such as in Figs. 6(c)−6(e). There was a small necking zone on the fracture surface of the 230-sample, as shown in Fig. 6(b), which was not found in the 190-sample. The phenomenon was consistent with the work-hardening exponential curve (Fig. 4(b)). There were many dimples in the necking zone, as seen in Fig. 6(f). This was another reason why the elongation of the 230-sample was greater than that of the other samples.

3.3. Wear resistance

The experimental results of the abrasive wear test are shown in Table 2. Under any of the experimental parameters of this study, the wear loss of the 190-sample was lower than that of the 210- and 230-samples. The wear losses of the 210- and 230-samples were essentially the same under low applied loads and low wear cycles. As the number of wear cycles or the applied load increased, the wear loss of the 210-sample was lower than that of the 230-sample. Weight loss of the samples was approximately linear with the cycles of wear, whereas the weight loss of the tested

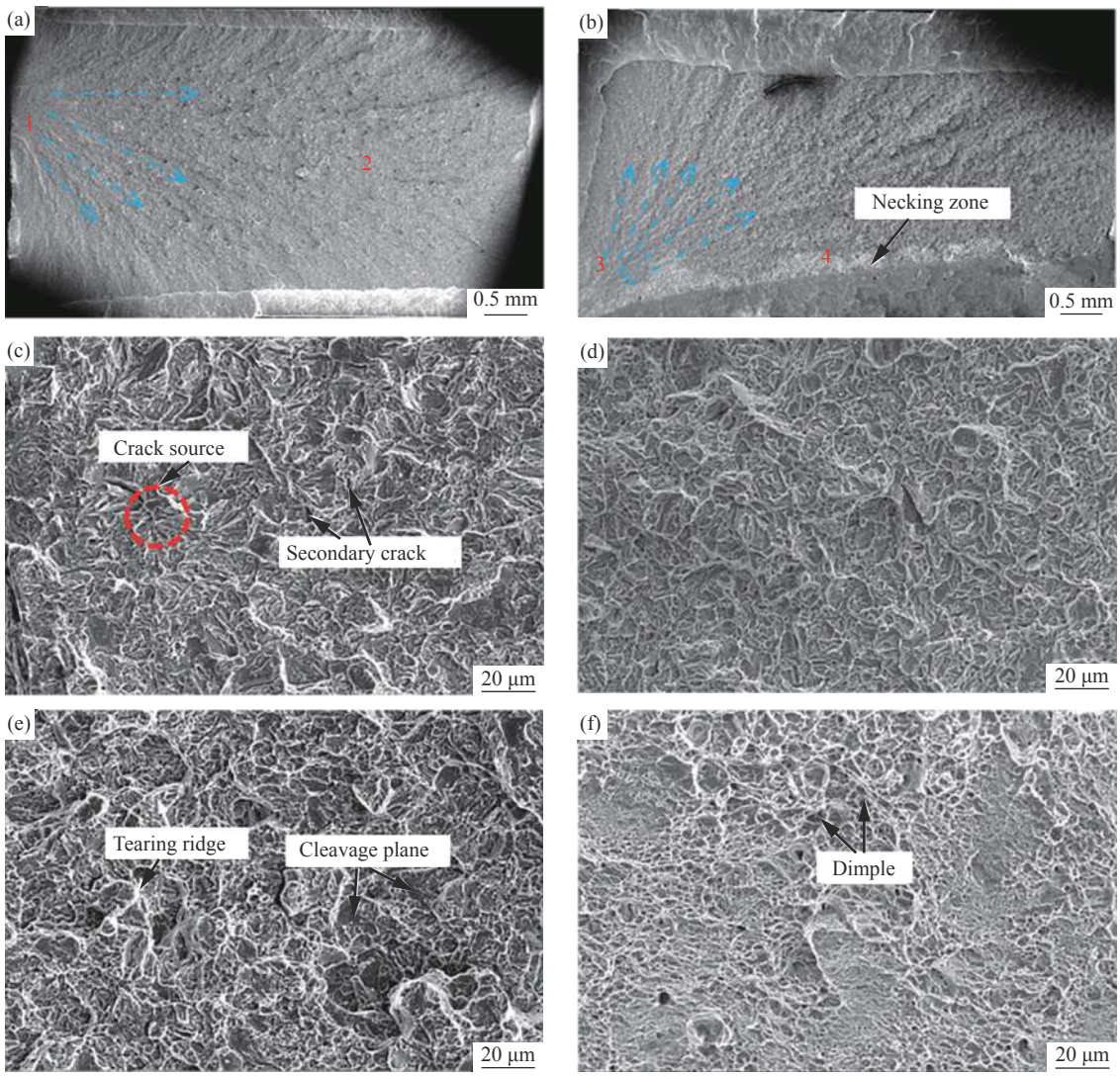

Fig. 6. Typical SEM micrographs of tensile fractures of the samples at (a) 190°C and (b) 230°C; (c) enlargement of area 1 in (a); (d) enlargement of area 3 in (b); (e) enlargement of area 2 in (a); (f) enlargement of area 4 in (b).

samples increased nonlinearly with increasing applied load under the same number of cycles, as shown in Table 2. Wear resistance of the tested samples increased with decreasing austempering temperature. When the load was 5 N, the weight loss every increasing 200 cycles (Δ') was almost unchanged under the same austempering temperature. Weight loss increased with increasing load under 200 cycles, but the weight loss per increasing 5-N load (Δ'') of the investigated samples decreased with increasing applied load.

Figs. 7–8 show the SEM images of the worn surfaces of the experimental samples under different cycles and loads.

Table 2. Weight loss of the samples under different heat treatments and different wear conditions mg

Sample	5-200	5-400		5-600		10-200		15-200	
	WL	WL	Δ'	WL	Δ'	WL	Δ''	WL	Δ''
190-sample	27.9 ± 1.4	58.4 ± 2.9	29.5 ± 1.5	84.1 ± 4.2	25.7 ± 1.3	41.0 ± 2.0	13.1 ± 0.6	50.5 ± 2.5	9.5 ± 0.5
210-sample	30.1 ± 1.5	61.9 ± 3.1	31.8 ± 1.6	88.1 ± 4.4	26.2 ± 1.3	44.0 ± 2.2	13.9 ± 0.7	52.0 ± 2.6	8.0 ± 0.4
230-sample	30.0 ± 1.5	62.3 ± 3.1	32.3 ± 1.6	94.7 ± 4.7	32.4 ± 1.6	50.0 ± 2.5	20.0 ± 1.0	65.0 ± 3.2	15.0 ± 0.7

Note: 5-200, 5-400, 5-600, 10-200, and 15-200 represent the different wear conditions, in each the former represents applied load, and the latter represents wear cycle; WL represents weight loss; Δ' represents the weight loss per increasing 200 wear cycles with the load of 5 N; Δ'' represents the weight loss per increasing 5-N load under 200 wear cycles.

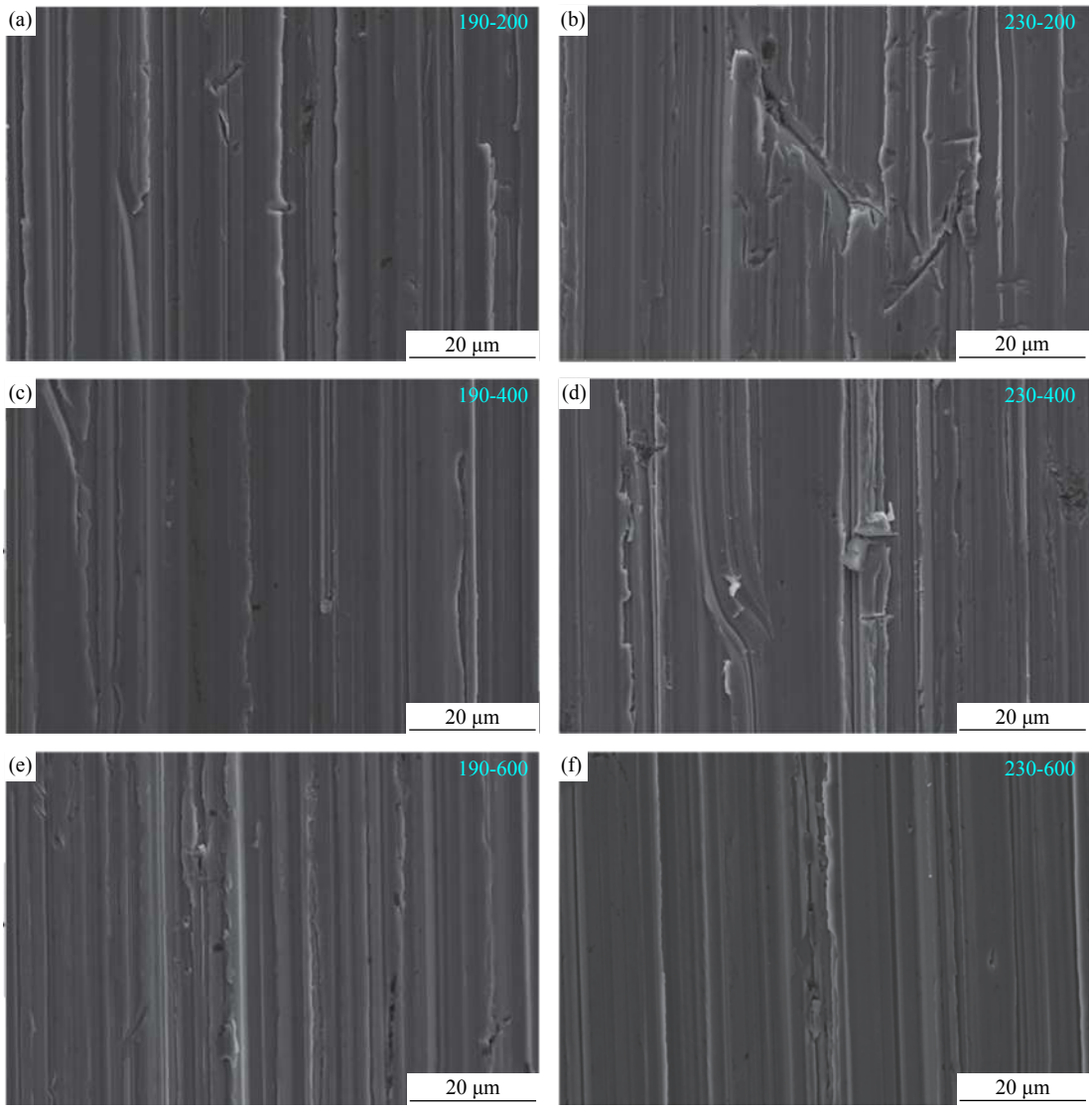

Fig. 7. SEM micrographs of the wear surface of austempered samples after abraded for different cycles under 5 N load. 190-200, 190-400, 190-600, 230-200, 230-400, and 230-600 represent the different wear conditions, in each the former represents austempering temperature, and the latter represents wear cycle.

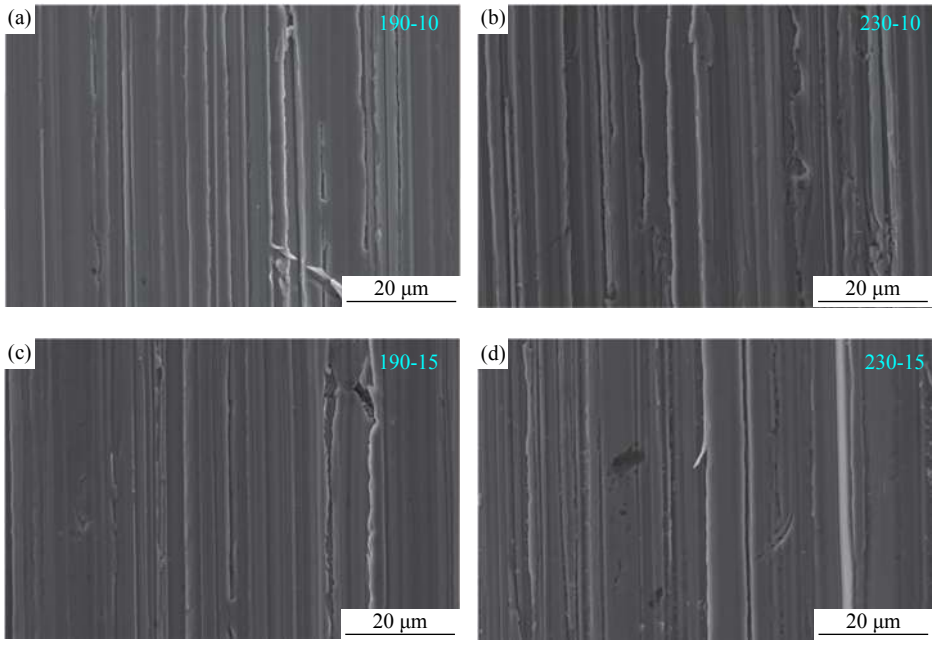

Fig. 8. SEM micrographs of the wear surface of austempered samples after abraded under the load of 10 and 15 N for 200 cycles. 190-10, 190-15, 230-10, and 230-15 represent the different wear conditions, in each the former represents austempering temperature, and the latter represents wear load.

Lengthwise cutting and continuous grooves were observed on the worn surface in all samples. The grooves were formed by SiC particles cutting the surface of samples. The direction of the grooves fell along the sliding route. The phenomenon indicated that the primary damage mechanism in this study was micro-plowing abrasion. It was noteworthy to observe that these processes endured very few material losses, as shown in Table 2. With increasing wear cycles and loads, the width of the grooves in the 190- and 230-samples increased, but the width of the grooves in the 190-sample was narrower than that of the 230-sample. The 230-sample under 200 and 400 cycles under 5 N presented some deep scratches, owing to the relatively low initial hardness ($HV_{1.0}$ 593 ± 17) of the samples, which resulted in some SiC particles being deeply pressed into the surface by the load. Straight grooves were most likely to be observed in other samples, because of the relatively high initial hardness ($HV_{1.0}$ 673 ± 20) of the 190-samples and the more-hardened layer of the 230-samples for 200 cycles, under 10 and 15 N.

Figs. 9−10 illustrate the line profiles of the wear surfaces with different samples by laser scanning confocal microscopy. The groove surfaces of the 190-samples having high initial hardness were "narrow and deep". With increasing wear cycles, the groove surfaces changed from "narrow and deep" to "wide and shallow", and then back to "narrow and deep". For samples having lower initial hardness, such as the 230-sample, the groove surfaces were "wide and shallow". With the increase in wear cycles, the surfaces of the grooves tended to be "narrow and deep". Similarly, the groove surfaces tended to be "narrow and deep" as the load increased. These results were consistent with those obtained by Narayanaswamy *et al.* [29].

Cross-sections of the worn surfaces of some samples under typical processes were observed by SEM, as shown in Fig. 11. A severely deformed layer was clearly seen between the worn surface and the violet dashed line. The deformed microstructures were rearranged and deflected in the sliding direction. Furthermore, in the deformed layer, the FRA became thinner and the BRA became slender. However, BRA was not observed to become FRA, which was inconsistent with the work of Singh *et al.* [19].

Generally, sliding abrasion involves high strain levels on the abrasive surface, resulting in severe deformation on the sub-surface of the samples during wear [30−31]. However, the thickness of the deformation layer varies. For example, in the 190-sample, the thickness of the deformation layer was close to zero with 200 wear cycles under 5 N (Fig. 11(a)). Under austempering at 230°C, the thickness of the deformation layer increased from 3 to 5 μm as the wear cycles increased from 200 to 600 (Figs. 11(e), 11(f), and 11(g)) with the same load of 5 N. When the number of wear cycles remained constant, the thickness of the deformation layer of the 190- and 230-samples increased with increasing applied loads (Figs. 11(a) and 11(d), and Figs. 11(e) and 11(h)).

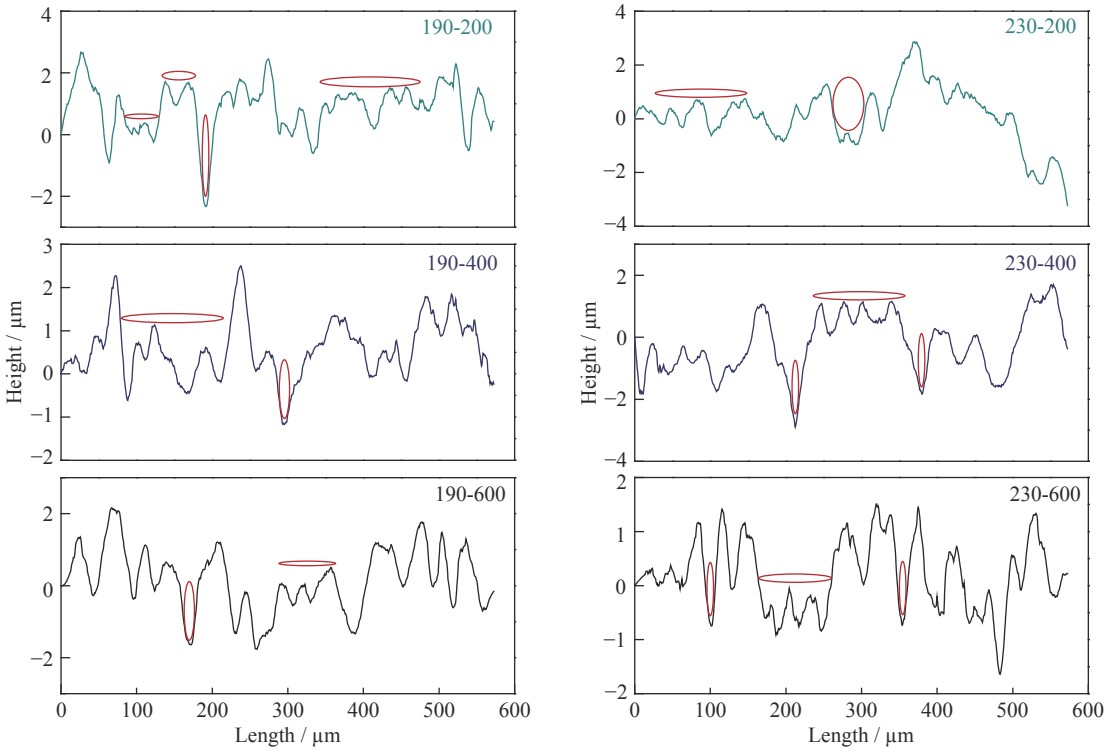

Fig. 9. Profiles of the wear surfaces of austempered samples after abraded for 200, 400, and 600 cycles under the load of 5 N. (190-200: the former represents austempering temperature (190°C), the latter represents wear cycle (200 cycles); 190-400, 190-600, 230-200, 230-400, and 230-600 are named the same way as 190-200).

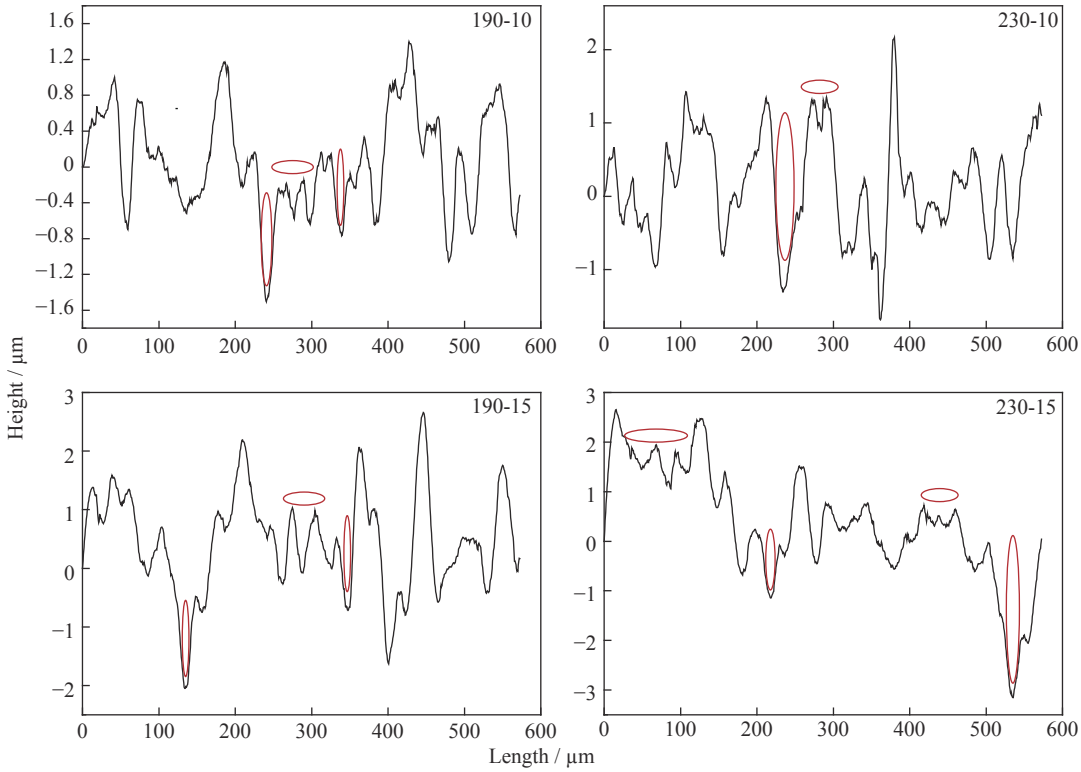

Fig. 10. Profiles of the wear surfaces of austempered samples after abraded under the load of 10 and 15 N for 200 cycles. (190-10: the former represents austempering temperature (190°C), the latter represents wear load (10 N); 190-15, 230-10, and 230-15 are named the same way as 190-10).

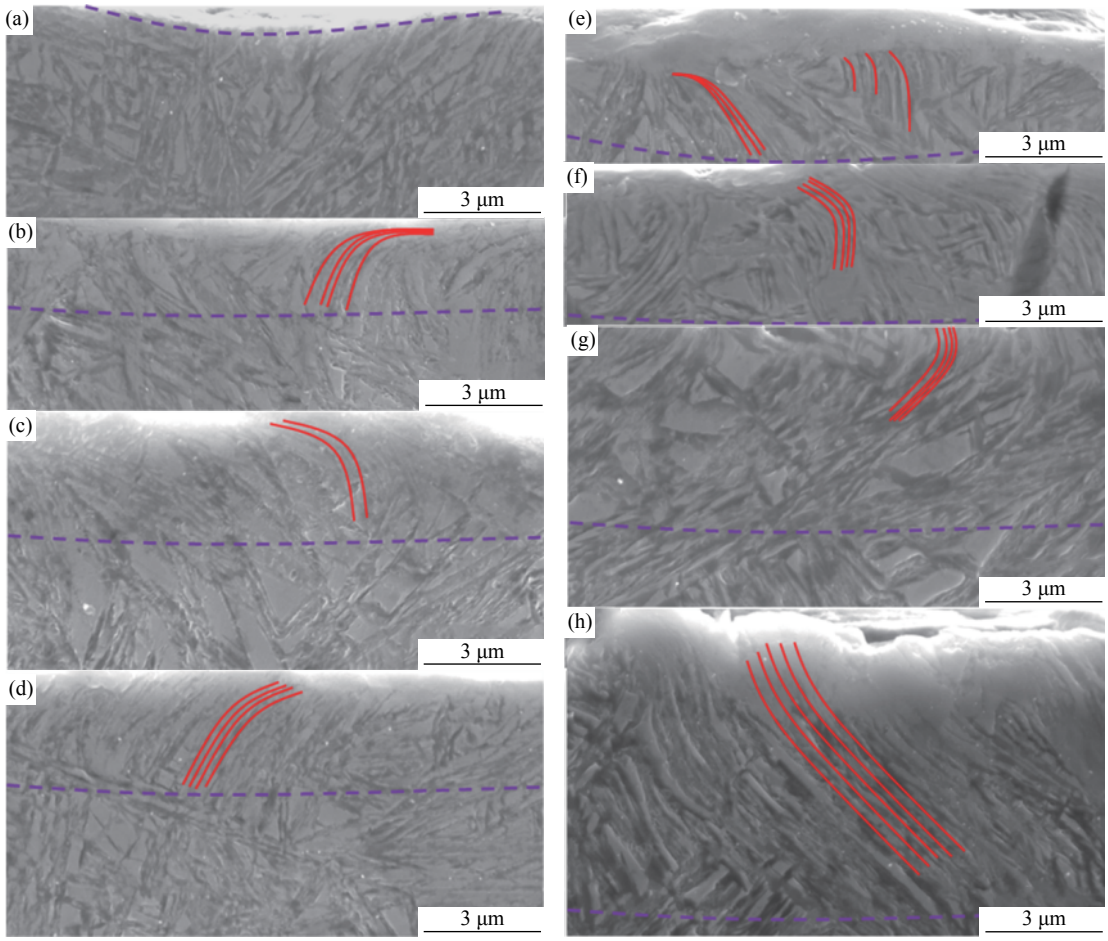

Fig. 11. SEM micrographs of wear sub-surface of different samples: (a–d) austempered at 190°C and with the wear condition of (a) 5 N, 200 cycles, (b) 5 N, 400 cycles, (c) 5 N, 600 cycles, and (d) 15 N, 200 cycles; (e–h) austempered at 230°C and with the wear condition of (e) 5 N, 200 cycles, (f) 5 N, 400 cycles, (g) 5 N, 600 cycles, and (h) 15 N, 200 cycles.

A non-etching layer beneath the surface was also observed, as shown in Fig. 11. This layer indicated the onset of wear matching with the location where, in theory, the maximum tangential traction stress occurs [17]. It was impossible to obtain martensitic transformation after reaustenitization at the mating surfaces during abrasion. Therefore, the non-etching layer became a typical reflection of intense, repeated deformation, grain fragmentation, and mechanical homogenization [32].

Compared with the 190-sample, the initial hardness of the 230-sample was lower. The pressure, therefore, propagated more deeply in the 230-sample under the same load, leading to a more significant deformation layer, as shown in Fig. 12. Liu *et al.* [33] found that the effect of RA stability was an essential factor in wear resistance. They reported that the RA stability decreased with increasing austempering temperature. When the mechanical stability of RA was high enough, it could delay the transformation of austenite to martensite. Therefore, compared with the 190-sample, it was easier for RA in the 230-sample to transform into martensite, thereby improving the surface hardness and enhancing the wear resistance.

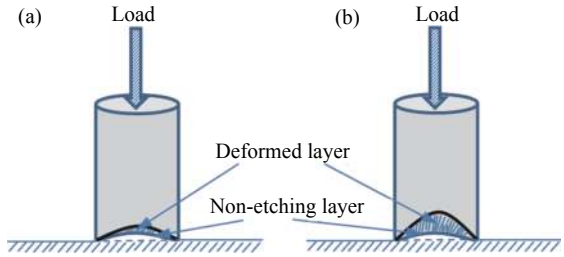

Fig. 12. Schematic diagram of wear mechanism: (a) 190-sample (with a higher hardness); (b) 230-sample (with a lower hardness).

4. Conclusions

This paper investigated the properties of ultrafine bainitic steel by isothermal transformation at temperatures as low

as between Ms + 5°C and Ms + 50°C, and the following conclusions can be drawn from the analysis of results.

(1) The tensile strength of samples austempered at 190–230°C was better than 1800 MPa, but the only sample austempered at 230°C had an elongation of more than 10%. The samples under different temperatures had high wear resistance because of the high initial hardness ($HV_{1.0}$ 593–673).

(2) The wear surface in ultrafine bainitic steel mainly comprises grooves, and micro-plowing is the main wear mechanism. As the austempering temperature decreases, the change in wear resistance is not significant. The sample weight loss was approximately linear with the cycles of wear, whereas the sample weight loss was nonlinear with the increase in applied loads.

(3) Under the same wear condition, the deformation layer thickness of 230-sample is higher than that of 190-sample. This phenomenon is related to the initial hardness of the sample and the stability of the RA.

Acknowledgements

This work was financially supported by the National Key Research and Development Plan of China (No. 2016YFB0300205) and the National Natural Science Foundation of China (Nos. U1810207 and 51601174).

References

[1] F.G. Caballero, H.K.D.H. Bhadeshia, K.J.A. Mawella, D.G. Jones, and P. Brown, Very strong low temperature bainite, *Meter. Sci. Technol.*, 18(2002), No. 3, p. 279.

[2] Z.W. Hu, G. Xu, H.J. Hu, L. Wang, and Z.L. Xue, *In situ* measured growth rates of bainite plates in an Fe−C−Mn−Si superbainitic steel, *Int. J. Miner. Metall. Mater.*, 21(2014), No. 4, p. 371.

[3] H.L. Fan, A.M. Zhao, Q.C. Li, H. Guo, and J.G. He, Effects of ausforming strain on bainite transformation in nanostructured bainite steel, *Int. J. Miner. Metall. Mater.*, 24(2017), No. 3, p. 264.

[4] A. Behzad, Effect of prolonged isothermal heat treatment on the mechanical behavior of advanced NANOBAIN steel, *Int. J. Miner. Metall. Mater.*, 24(2017), No. 9, p. 1010.

[5] J. Zhao, K. Guo, Y.M. He, Y.F. Wang, and T.S. Wang, Extremely high strength achievement in medium-C nanobainite steel, *Scripta Mater.*, 152(2018), p. 20.

[6] J.G. He, A.M. Zhao, C. Zhi, and H.L. Fan, Acceleration of nanobainite transformation by multi-step ausforming process, *Scripta Mater.*, 107(2015), p. 71.

[7] H. Guo, X.Y. Feng, A.M. Zhao, Q. Li, and J. Ma, Influence of prior martensite on bainite transformation, microstructures, and mechanical properties in ultra-fine bainitic steel, *Materials*, 12(2019), No. 3, p. 527.

[8] A. Kumar and A. Singh, Toughness dependence of nanobainite on phase fraction and morphology, *Mater. Sci. Eng. A*, 729(2018), p. 439.

[9] M.N. Yoozbashi, S. Yazdani, and T.S. Wang, Design of a new nanostructured, high-Si bainitic steel with lower cost production, *Mater. Des.*, 32(2011), No. 6, p. 3248.

[10] X.H. Lu, D.S. Qian, W. Li, and X.J. Jin, Enhanced toughness of bearing steel by combining prior cold deformation with martensite pre-quenching and bainite transformation, *Mater. Lett.*, 234(2019), p. 5.

[11] H. Guo, A.M. Zhao, C. Zhi, R. Ding, and J.X. Wang, Two-body abrasion wear mechanism of super bainitic steel, *Mater. Sci. Technol.*, 33(2017), No. 7, p. 893.

[12] V.G. Efremenkoa, O. Hesse, T. Friedrich, M. Kunert, M.N. Brykov, K. Shimizu, V.I. Zurnadzhy, and P. Šuchmann, Two-body abrasion resistance of high-carbon high-silicon steel: Metastable austenite vs nanostructured bainite, *Wear*, 418-419(2019), p. 24.

[13] S. Das Bakshi, P.H. Shipway, and H.K.D.H. Bhadeshia, Three-body abrasive wear of fine pearlite, nanostructured bainite and martensite, *Wear*, 308(2013), No. 1-2, p. 46.

[14] M. Shah and S. Das Bakshi, Three-body abrasive wear of carbide-free bainite, martensite and bainite-martensite structure of similar hardness, *Wear*, 402-403(2018), p. 207.

[15] T.S. Wang, J. Yang, C.J. Shang, X.Y. Li, B. Lv, M. Zhang, and F.C. Zhang, Sliding friction surface microstructure and wear resistance of 9SiCr steel with low-temperature austempering treatment, *Surf. Coat. Technol.*, 202(2008), No. 16, p. 4036.

[16] S.M. Hasan, D. Chakrabarti, and S.B. Singh, Dry rolling/sliding wear behaviour of pearlitic rail and newly developed carbide-free bainitic rail steels, *Wear*, 408-409(2018), p. 151.

[17] S. Das Bakshi, A. Leiro, B. Prakash, and H.K.D.H Bhadeshia, Dry rolling/sliding wear of nanostructured bainite, *Wear*, 316(2014), No. 1-2, pp. 70-78.

[18] R. Rementeria, I. García, M.M. Aranda, and F.G. Caballero, Reciprocating-sliding wear behavior of nanostructured and ultra-fine high-silicon bainitic steels, *Wear*, 338-339(2015), p. 202.

[19] K. Singh and A. Singh, Tribological response and microstructural evolution of nanostructured bainitic steel under repeated frictional sliding, *Wear*, 410-411(2018), p. 63.

[20] X.Y. Long, F.C. Zhang, J. Kang, Z.N. Yang, D.D. Wu, K.M. Wu, and G.H. Zhang, Study on carbide-bearing and carbide-free bainitic steels and their wear resistance, *Mater. Sci. Technol.*, 33(2017), No. 5, p. 615.

[21] A.K. De, D.C. Murdock, M.C. Mataya, J.G., Speer, and D.K. Matlock, Quantitative measurement of deformation-induced martensite in 304 stainless steel by X-ray diffraction, *Scripta Mater.*, 50(2004), No. 12, p. 1445.

[22] H.K.D.H. Bhadeshia and D.V. Edmonds, Bainite in silicon steels: New composition-property approach Part 1, *Met. Sci.*, 17(1983), No. 9, p. 411.

[23] E. Kozeschnik and H.K.D.H. Bhadeshia, Influence of silicon on cementite precipitation in steels, *Mater. Sci. Technol.*, 24(2008), No. 3, p. 343.

[24] L.C. Chang and H.K.D.H. Bhadeshia, Austenite films in bainitic microstructures, *Mater. Sci. Technol.*, 11(1995), No. 9, p. 874.

[25] C. Garcia-Mateo, F.G. Caballero, T. Sourmail, M. Kuntz, J. Cornide, V. Smanio, and R. Elvira, Tensile behaviour of a nanocrystalline bainitic steel containing 3wt% silicon, *Mater. Sci. Eng. A*, 549(2012), p. 185.

[26] C. Garcia-Mateo, F.G. Caballero, and H.K.D.H. Bhadeshia, Acceleration of low-temperature bainite, *ISIJ Int.*, 43(2003), No. 11, p. 1821.

[27] B. Avishan, M. Tavakolian, and S. Yazdani, Two-step austempering of high performance steel with nanoscale microstructure, *Mater. Sci. Eng. A*, 693(2017), p. 178.

[28] J. Chiang, B. Lawrence, J.D. Boyd, and A.K. Pilkey, Effect of microstructure on retained austenite stability and work hardening of TRIP steels, *Mater. Sci. Eng. A*, 528(2011), No. 13-14, p. 4516.

[29] B. Narayanaswamy, P. Hodgson, I. Timokhina, and H. Beladi, The impact of retained austenite characteristics on the two-body abrasive wear behavior of ultrahigh strength bainitic steels, *Metall. Mater. Trans. A*, 47(2016), No. 10, p. 4883.

[30] J. Larsen-Basse, Role of microstructure and mechanical properties in abrasion, *Scripta Metall. Mater.*, 24(1990), No. 5, p. 821.

[31] T. Sun, R.B. Song, F.Q. Yang, and C.J. Wu, Wear behavior of bainite ductile cast iron under impact load, *Int. J. Miner. Metall. Mater.*, 21(2014), No. 9, p. 871.

[32] H.K.D.H. Bhadeshia, Steels for bearings, *Prog. Mater. Sci.*, 57(2012), No. 2, p. 268.

[33] B.G. Liu, W. Li, X.W. Lu, X.S. Jia, and X.J. Jin, The effect of retained austenite stability on impact-abrasion wear resistance in carbide-free bainitic steels, *Wear*, 428-429(2019), p. 127.